Removal of Astrazon Red Dye from Wastewater using Eggshell/Graphene Oxide Embed in (Gum Acacia/Acrylamide) Hydrogel Nanocomposites Synthesized by Gamma Irradiation

Nehad A. Ahmed[1] · Mai F. Elshahawy[1] · Randa D. Mohammed[1] · Ghada A. Mahmoud[1] 🔵

Abstract

This research aimed to use a low-cost, environmentally friendly adsorbent to eliminate the cationic dye Astrazon red 6B (AR) from an aqueous system. For this rationale, a nanocomposite hydrogel made of (Gum Acacia/Acrylamide)-calcinated Eggshell/Graphene oxide (GA/AAm)-ES/GO was created using Gamma radiation-induced copolymerization and cross-linking. FT-IR, XRD, EDX mapping, SEM, TGA and TEM were used to investigate the structures and properties. The nanocomposites exhibited superior adsorption behavior towards AR. Because of the dual effect of ES and GO, mixing ES with GO in (GA/AAm)-ES/GO nanocomposite hydrogel improved its adsorption capability. It was obtained that the optimum initial pH was 9 and the equilibrium contact time was 480 min. The removal percentage was enhanced by increasing the initial dye concentration. A little removal effectiveness was observed by increasing the adsorbent weight from 5.0 to 10.0 g for each liter of the dye solution. The Langmuir isotherm was found to be more suitable for analyzing the adsorption isotherm the maximal monolayer dye adsorption capacity (q_{max}) was 313.3 mg/g. The pseudo-second-order adsorption kinetics fitted the data well, and the rate constant was predicted to be (0.108×10^{-3}) g mg^{-1} min^{-1}. $\Delta H°$ values are negative at all investigated initial concentrations for (GA/AAm)-ES and (GA/AAm)-ES/GO. The values of $\Delta S°$ are negative for (GA/AAm)-ES/GO, while values for (GA/AAm) and (GA/AAm)-ES are positive. $\Delta G°$ are negative values for all systems that refer to the spontaneity of the adsorption process. High efficiency was observed for (GA/AAm)-ES/GO up to three rounds of reuse, while a drop in efficiency of the fourth round to 58.78%.

✉ Ghada A. Mahmoud
 ghadancrrt@yahoo.com

1 Polymer Chemistry Department, National Center for Radiation Research and Technology, Egyptian Atomic Energy Authority, Cairo, Egypt

Graphical Abstract
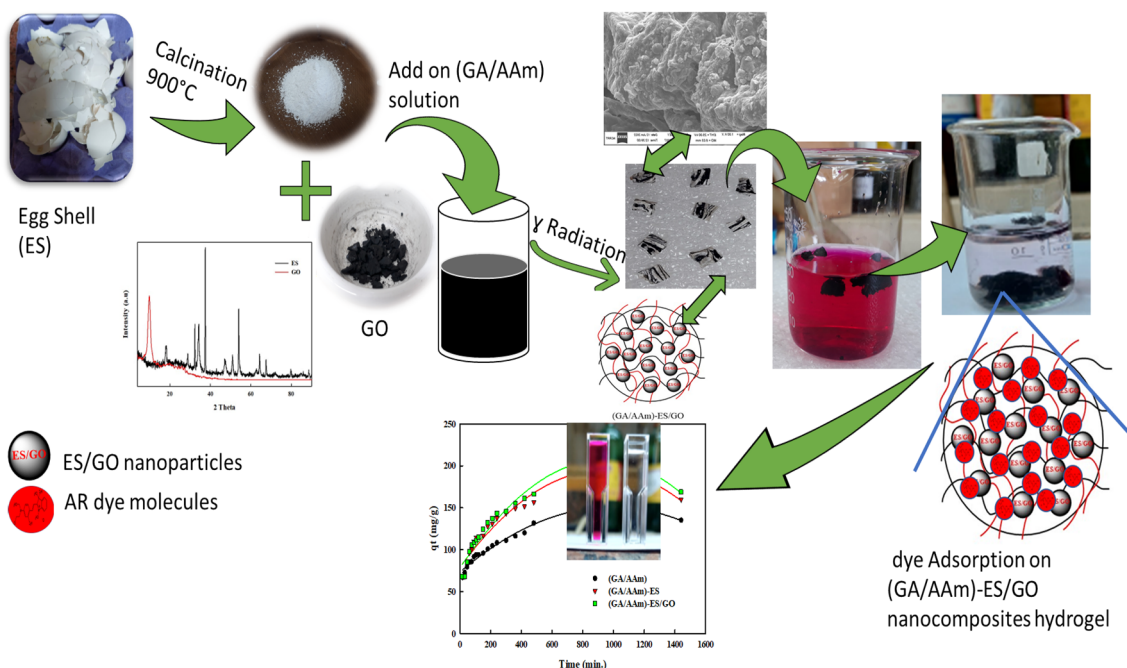
1 Introduction

Water is considered the most crucial natural material for beings [1]. Dye-related water contamination is still a significant environmental and social issue in our society [2]. Dyes are a significant class of pollutants that were produced in large quantities by numerous industries [3]. Some dyes are hazardous and even carcinogenic, even in low concentrations, affecting photosynthetic activity, aquatic biota, human health, and the ecosystem [4]. Cationic dyes, such as Astrazon red 6B, are dangerous and damaging to humans and aquatic habitats [5]. Many studies have been conducted to eliminate dye effluents from wastewaters, including coagulation, photocatalytic oxidation, adsorption, Fenton/photo-Fenton, biological, and physical–chemical methods [6]. The adsorption process is one of the important techniques for eliminating dye pollutants due to its many benefits [7]. Egg Shell (ES) is the hard outer shell of eggs and contains a large amount of CaO, which is produced in large quantities as a daily waste [1]. Adsorbents derived from natural waste, such as eggshells (ES) are highly considered [8]. Because of its porous nature, ES is an appealing material for use as an efficient adsorbent [9]. ES is being doped with active carbon materials such as graphene oxide (GO) to boost the adsorption efficiency [10]. GO has unique properties such as easy combinability

with other materials, high specific surface area, and high heat transfer [2]. It is considered among the most efficient doped materials. GO is rich in active oxygen (hydroxyl, epoxy, and carboxyl) groups, allowing it to be used in water remediation [11]. To make handling and reusing the Es/GO nanocomposites for dye adsorption easier, they are entrapped in polymeric materials such as hydrogels with specific properties such as high swelling, good mechanical strength, and durability without dissolving in different solutes [12]. Hydrogels are cross-linked polymer chains that can retain huge quantities of water without dissolving [13]. The occurrence of active groups such as –OH, –COOH, and –CONH establishes hydrogels' hydrophilic nature. They are regarded as promising adsorbents for organic dyes removal, on account of high water content and the facility of incorporating different chelating groups onto the polymeric backbones. Gum acacia, also known as gum arabic, is a natural polysaccharide that is derived from the sap of the acacia tree. It is a water-soluble, non-toxic, and biodegradable polymer that has been used in a wide range of applications [3], 14. Gum acacia hydrogels have also been explored for their potential in adsorption applications. Due to their high water absorption capacity and biocompatibility, gum acacia hydrogels have been used as an adsorbent for various contaminants, such as heavy metals, dyes, and organic pollutants [4]. GA is copolymerized

with different vinyl group monomers such as acrylamide (AAm) to increase its durability [5].

The radiation technology is eco-friendly, with less contamination and fewer byproducts that are used in the preparation and crosslinking of hydrogels [15]. The irradiation of polymeric materials with ionizing radiation leads to the formation of very reactive intermediates, free radicals, ions and excited states. These intermediates can follow several reaction paths that result in disproportion, arrangements and/ or the formation of new bonds.

In this study the creation of a nanocomposite for the first time composed of GA/AAm including calcinated Eggshell ES and graphene oxide GO, (GA/AAm)-ES/GO, using a gamma irradiation approach was the major focus of this work to adsorptive removal of the AR from aqueous solutions.

2 Materials and Procedures

Gum Acacia (GA) was supplied from OXFORD laboratory reagent (India) with a purity of 96%. Acrylamide (AAm) was supplied from Central Drug House (CDH) (India) with a purity of 98%. Graphite powder (GP) was received from Loba Chemie (India) with a purity of 96%. Sodium hydroxide, hydrochloric acid, sulfuric acid, phosphoric acid, sodium nitrate, Potassium permanganate, and hydrogen peroxide were provided by El Nasr Pharmaceutical Chemicals Co. (Egypt) with a purity of 98%. Astrazon red 6B (AR) ($C_{24}H_{30}Cl_2N_2$) Fig. 1 was obtained from El-Gomhouria Co. (Egypt).

2.1 Synthesis of GO

GO was manufactured from GP using the modified Hummer's procedure [16]. For 10 min, an ice bath was used to stir up a mixture of GP (5 g), $NaNO_3$ (2.5 g), H_2SO_4 (108 mL), and H_3PO_4 (12 mL). 15 g of KMnO4 was gradually added while holding the temperature below 5 °C in an ice bath. The $NaNO_3$ acts as a source of nitrate ions, which helps to increase the solubility of graphite in the reaction mixture. The H_2SO_4 and H_3PO_4 are strong acids that promote the oxidation of graphite to graphene oxide. The $KMnO_4$

is a powerful oxidizing agent that helps to break down the graphite into smaller pieces, which promotes the formation of graphene oxide [6, 7]. The solution was allowed to react for two hours. In a water bath, the temperature was increased to 40 °C for 60 min while stirring continuously. The mixture was then heated to 98 °C for 60 min while deionized water was gradually added until the suspension solution volume reached 400 mL and after five minutes. The reaction product is rinsed several times with 5% HCl solution, deionized water, and dried at 60 °C.

2.2 Synthesis of Egg Shell Nanoparticles (ES)

Eggshells ES were collected from local shops. 50 g of ES were cleaned with deionized water to remove impurities before being inserted in a dry oven at 110 °C for two hours. ES was then calcinated at 1100 °C for four hours in a muffle furnace. The solid generated from ES was calcined, then cooled for 10 h in the furnace before being kept in a desiccator [17].

2.3 Preparation of (GA/AAm) Hydrogel, (GA/AAm)-ES, and (GA/AAm)-ES/GO Nanocomposite

Homogeneous aqueous solutions of AAm and GA mixture of different compositions at different total feed concentrations 10, 20, 30, and 40 wt % were irradiated in small glass vials by ^{60}Co gamma rays at irradiation doses of 15, 25, and 35 kGy. The produced polymeric cylinders were cut into discs of 2 mm thickness. All samples were washed to confiscate the homopolymer before being air dried.

The (GA/AAm)-ES and (GA/AAm)-ES/GO nanocomposite hydrogels were created by combining different weights of ES or ES/GO (1:1) with (GA/AAm) (3/7) wt% solution of total concentration 30 wt% in a probe sonicator. The homogeneous solutions were then revealed to gamma radiation at 35 kGy to form the various nanocomposite hydrogels.

2.4 Instrumentations

X-ray diffraction (XRD) was done using XD-DI Series, Shimadzu apparatus with a copper target (k = 1.542 Å) at an operating voltage of 40 kV and an electric current of 30 mA. The patterns were done at ambient temperature and under constant conditions.

The interlayer spacing d of GO was determined by Bragg's law, Eq. (1): [18]

$$n\lambda = 2d \sin \theta \qquad (1)$$

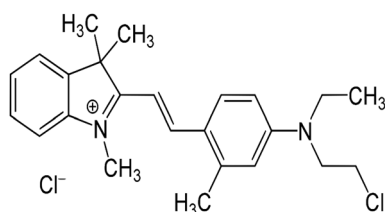where n is the diffraction series and λ is the X-ray wavelength.

Fig. 1 The Chemical structure of Astrazon red 6B dye

FTIR spectroscopy measurement was done using Nicolet Is10 FT-IR within a range of 400–4000 cm^{-1} using KBr pellets. TEM investigation was done by a transmission electron microscope (TEM) Thermo scientific Talos F200i scanning/transmission. The surface morphology and energy dispersive analysis of X-ray (EDX) were examined on SEM apertures (ZEISS EVO-15, UK) with attached EDX. Thermogravimetric analysis (TGA) system of Type TGA-50 under nitrogen atmosphere was used to determine the thermal stability and weight loss of the prepared hydrogels and composites as a function of temperature. The temperature ranged from ambient to 600 °C at a heating rate of 10 °C/min.

2.5 Adsorption Studies

The adsorption of the aqueous solution of Astrazon 6B dye (AR) was performed by preparing a stock solution of 1,000 mg/L AR dye. Definite concentrations were made by the dilution. The dye's UV–Visible absorption spectra were taken at $\lambda = 548$ nm using a UV–Vis spectrophotometer (TU-1901, Beijing, China). The removal efficiency (R, %), the amount of AR dye adsorbed at time t (qt, mg/g), and equilibrium (qe, mg/g) was calculated by the following equations:

$$R = \frac{C0 - Ct}{C0} \times 100 \tag{2}$$

$$qt = \frac{C0 - Ct}{m} \times V \tag{3}$$

$$qe = \frac{C0 - Ce}{m} \times V \tag{4}$$

where C_0, C_t, and C_e (mg/L) are the initial, at time t, and equilibrium concentration of AR dye, respectively. V (L) is the volume of the solution and m (gram) is the weight of the adsorbent [17, 19].

3 Result and Discussion

3.1 Description of GO and ES

Figure 2 depicts the XRD analysis of GO and ES. The GO diffraction peak appears at 11.3° and of 0.778 nm interlayer distance of (Eq. 1). It is thought to be responsible for the formation of oxygen-containing groups in GO as a result of chemical oxidation and exfoliation, as well as the expansion of GO sheets [20]. The signature peaks of ES are revealed in Fig. 2, with intense distinguishing diffraction peaks. Peaks at 28.88° with miller indices (102) is attributed to Ca(CO$_3$)$_2$ remaining in ES and the diffraction peaks at 34.37°, and 54.53° were caused by the cubic CaO crystals according to

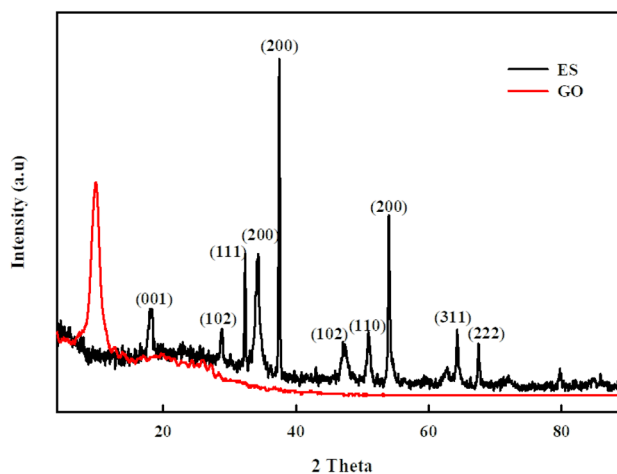**Fig. 2** XRD patterns of ES shell and GO

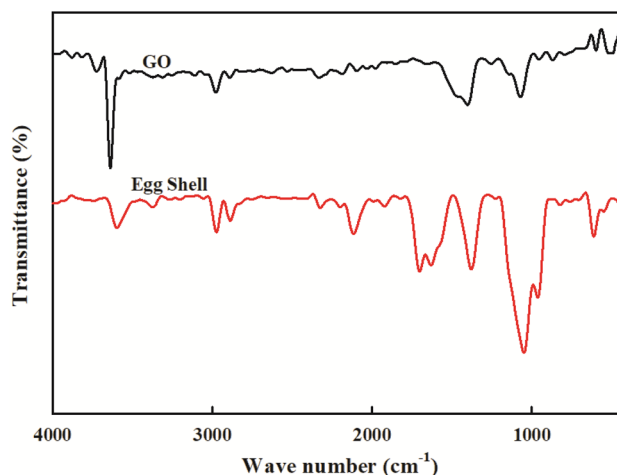**Fig. 3** FTIR spectra of GO and ES

miller indices (200), and (200) respectively and 2θ of 18.29°, 47.48°, and 51.11° with miller indices (001), (102), and (110) respectively, were caused by the presence of hexagonal calcium hydroxide in ES [21–23]. The peaks at 32.12°, 37.14°, 64.2°, and 67.41°, with miller indices, (111), (200), (311) and (222) confirmed the cubic crystallographic planes of CaO in ES [24].

TIR spectra scrutinize the functional groups extant on the prepared GO and ES are seen in Fig. 3. The spectrum of GO showed a broad peak around 3597.91 cm^{-1}, and peaks at 2975.73 and 2888 cm^{-1} were scribed to the O–H, –CH$_2$ and –C–H stretching vibrations, respectively [25]. The distinguishing peak at 1703.11 cm^{-1} is due to the C=O group in GO, and the peak at 1632.68 cm^{-1} is related to the aromatic C–C skeletal vibrations. The peaks at 1379 cm^{-1} and 1044 cm^{-1} are official to C–OH and C–O–C, respectively, which revealed the oxidation's success [26]. For ES, the

peak at 3638.74 cm^{-1} revealed the stretching vibration of O–H present in Ca(OH)$_2$. Furthermore, the (OH) of physiosorbed water linked to nanoparticles and its formation possibly arises from the adsorption of CaO with H$_2$O [27]. The small transmission bands at 2978.50 cm^{-1}, 1407.55 cm^{-1}, and 1071.68 cm^{-1} indicated to the carbonate CO$_3^{2-}$ ions in calcium carbonate CaCO$_3$ molecule, which reveals the carbonate is a base composition of eggshell [27]. The peaks at 599.94 and 495.07 cm^{-1} are associated with CaO vibration [28].

Figure 4 show the EDX elemental mapping images of ES and GO. As shown in Fig. 4a, ES analysis demonstrated the presence of elements O, Mg, P, and Ca. The elemental analysis revealed that the calcium content is 59.89%, the oxygen content is 39.17%, and there are traces of magnesium and phosphorus. The GO EDX analysis revealed that the carbon content is 56.35% and the oxygen content is 43.56% as seen in Fig. 4b.igure 5 shows the TEM morphology of ES and GO. The GO seems to as thin wrinkles sheets, Fig. 5a. Additionally, the wrinkled sheets stop the GO from clumping together by van der Waals forces through drying [29, 30]. TEM image of ES appears as particle agglomeration with round, flower, and irregular shapes morphology as shown in Fig. 5b. The large average size may be due to the calcination process at 900 °C. The higher temperature produced more atomic diffusion and higher energy [31].

3.2 Radiation Synthesis of (GA/AAm) Hydrogel

Gamma radiation is a clean tool, which is considered a source of initiation and cross-linking reaction. γ-radiation was used to graft copolymerization of AAm onto the GA chain for producing the functional polymeric hydrogel of (GA/AAm). Upon the acquaintance of the aqueous mixture of GA polymer and AAm monomer to γ irradiations. Water undergoes radiolysis, producing OH• radicals that extract H atoms from GA chains to produce macroradicals. Also, the γ- radiation cleaves the vinyl bond in the AAm monomer yielding the AAm• radicals, which is considered the initiation step for the free radical polymerization reaction. Then recombination of the free radicals produces new covalent bonds between the GA macroradical chains and the AAm• moieties and the formation of an insoluble fraction of (GA/AAm) hydrogel [7]. The possible mechanism of formation (GA/AAm) hydrogel is shown in Fig. 6.The effect of total GA/AAm feed concentration on the gelation of (GA/AAm) hydrogel at three different irradiation doses was illustrated in Fig. 7a. The gel content percent was enhanced by raising the total feed concentration and increasing the irradiation dose. Because the radicals become closer to each, facilitating the recombination, improving the crosslinking density, and enhancing the gel content percent [32]. On the other hand, the longtime exposure to gamma irradiation permits

the formation of radicals on GA and AAm. Furthermore, the longtime exposure to gamma irradiation allows high radical formation on GA and AAm, which enhances a lot of radicals recombination and high crosslinking matrix and increases gel content percent [33]. The effect of AAm content on gel content percent is described in Fig. 7b. The gel content percent was improved by increasing the AAm content. This is because the intensification of –C=C groups in AAm chains generates free radicals, which enhances the crosslinking density in the (GA/AAm) hydrogel and the gel percent [34].

4 Swelling Behavior of (GA/AAm) Hydrogel

The effect of various parameters on swelling percent is shown in Fig. 8. The decrement in swelling percent of (GA/AAm) hydrogel with increasing the total feed concentration and irradiation dose Fig. 8a is due to the increase of the crosslinking formation that restricted the diffusion of water molecules into the hydrogel network [35]. The longtime exposure to gamma irradiation and high total feed concentration resulted in a decrement in the swelling percent due to the highly crosslinking density formation [36]. The increase of crosslinking density compacts the free volume available for swelling as well as limited positions that are ready for the diffusion of water and hindered by network structure formation [37]. On the other hand, the increase of AAm concentration in the feed composition also decreased the swelling percent of (GA/AAm) hydrogel (Fig. 8b) due to an increase the vinyl group content enhancing the crosslinked network structure of the (GA/AAm) hydrogel [38].

### 4.1 Effect of ES/GO Concentration on Gel Content and Swelling Percent

Figure 9 depicts the effect of incorporating ES and ES/GO nanoparticles in (GA/AAm) hydrogel on gel content and swelling percentage. The insert of nanoparticles (20 wt%) in the hydrogel network decreases the gel content percent from 95 for (GA/AAm) to 80 for (GA/AAm)-ES and 75% for (GA/AAm)-ES/GO nanocomposites. The nanoparticles weaken the network density, which decreases the gel content percentage, Fig. 9a. On the other hand, the loading of ES or ES/GO NPs throughout the (GA/AAm) hydrogel matrix causes an increment of swelling percent that was increased with the increase of the amount of ES or ES/GO nanoparticles, Fig. 9b. The inclusion of ES or ES/GO nanoparticles into the gel networks increases the hydrophilicity in the (GA/AAm) hydrogel network, allowing more water molecules to enter the hydrogel matrix. Furthermore, the nanoparticles have various sizes and surface charges that lead to absolute network expansion [39]. Moreover, ES or ES/GO
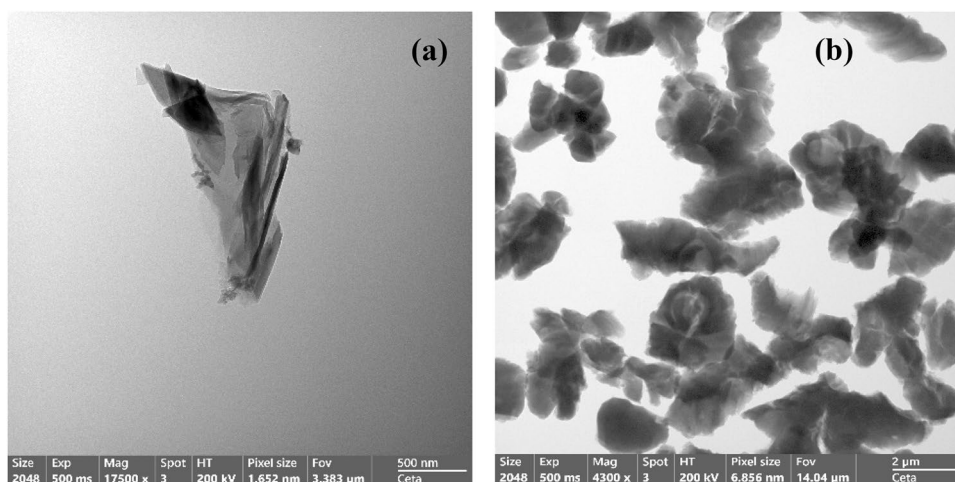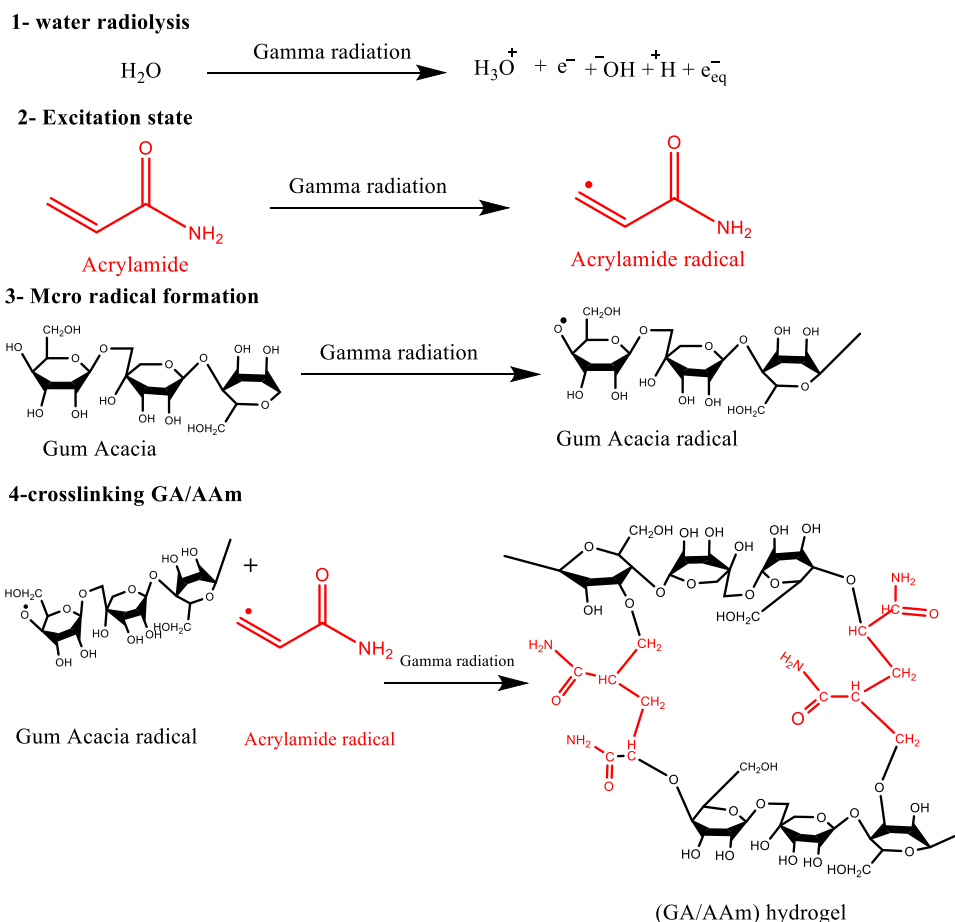
Fig. 4 a EDX mapping and elemental analysis of ES. **b** EDX mapping and elemental analysis of GO
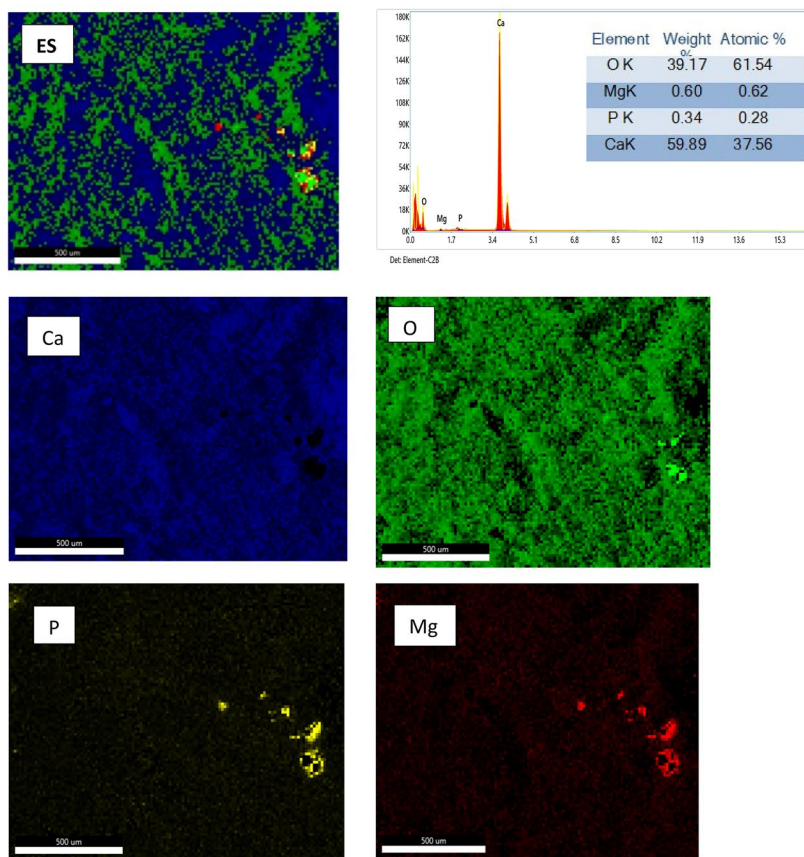
(a)
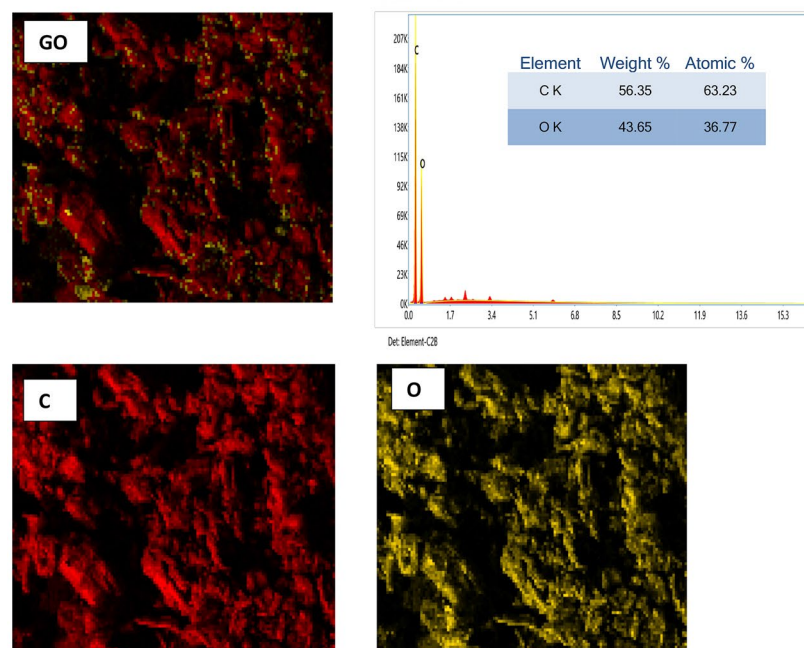

(b)

Fig. 5 TEM images **a** GO and **b** ES

Fig. 6 The possible mechanism of formation (GA/AAm) hydrogel

(GA/AAm) hydrogel

nanoparticles may increases the holes in (GA/AAm) hydrogel, increasing water molecule penetration in the hydrogel network [40].

4.2 Structure Study

Figure 10 shows the FTIR characteristic peaks spectra of (GA/AAm), (GA/AAm)-ES, and (GA/AAm)-ES/ GO nanocomposite hydrogels. For (GA/AAm) hydrogel, the asymmetric vibration peak of $–NH_2$ of AAm overlapped with the –OH stretching peak of GA seems around 3130 cm^{-1}. The bands for C-H and C$=$O appear at 2912 cm^{-1} and 1660 cm^{-1}, respectively. The bending vibration of the amide's –N–H bond was identified as a peak at 1413 cm^{-1}. The stretching vibrations of the C–O–C connect different sugar units of GA and appear at 1217
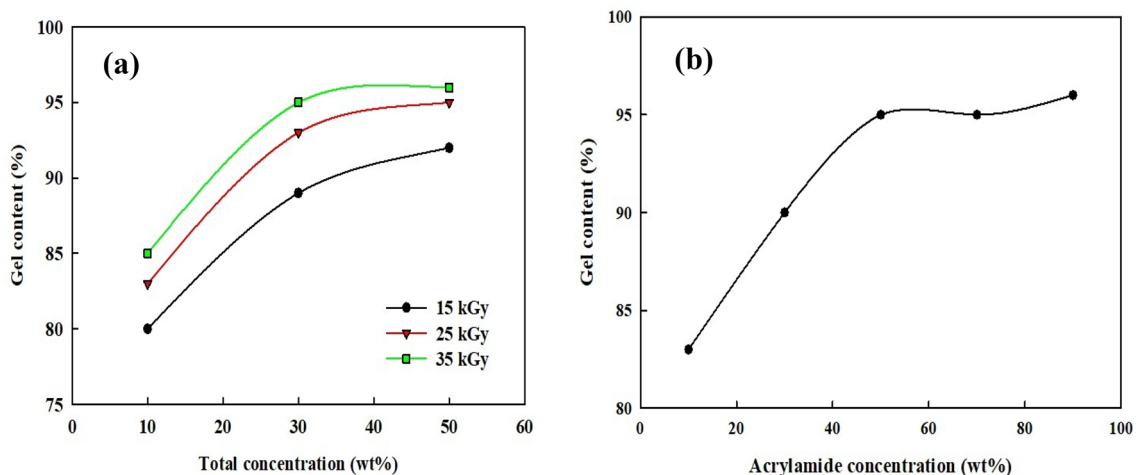
Fig. 7 Effect of **a** total concentration in the feed solution on the gel content percent of (GA/AAm) hydrogel at composition (3:7) wt% at different irradiation doses;15, 25 and 35 kGy, **b** effect of AAm con- centration on the gel content percent of (GA/AAm) hydrogel at total feed concentration; 30 wt% and irradiation dose; 35 kGy
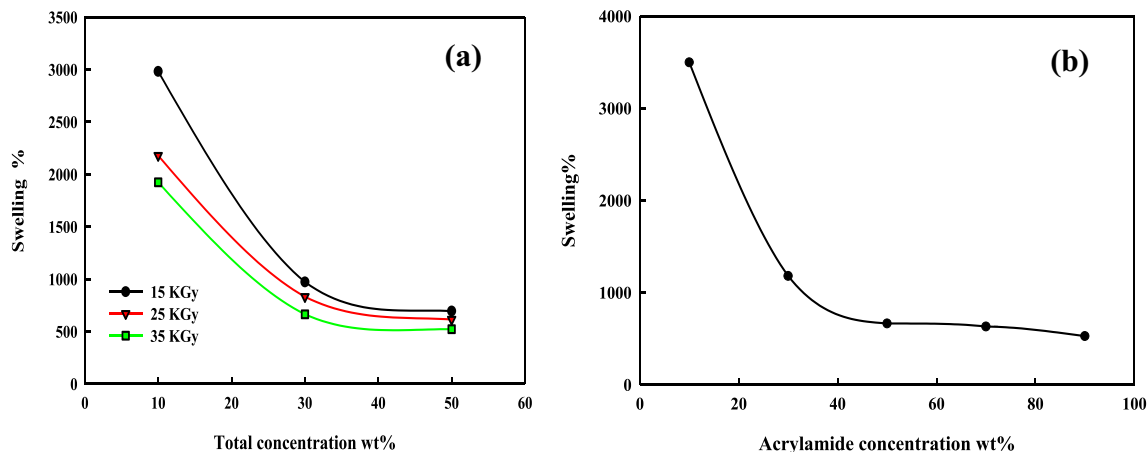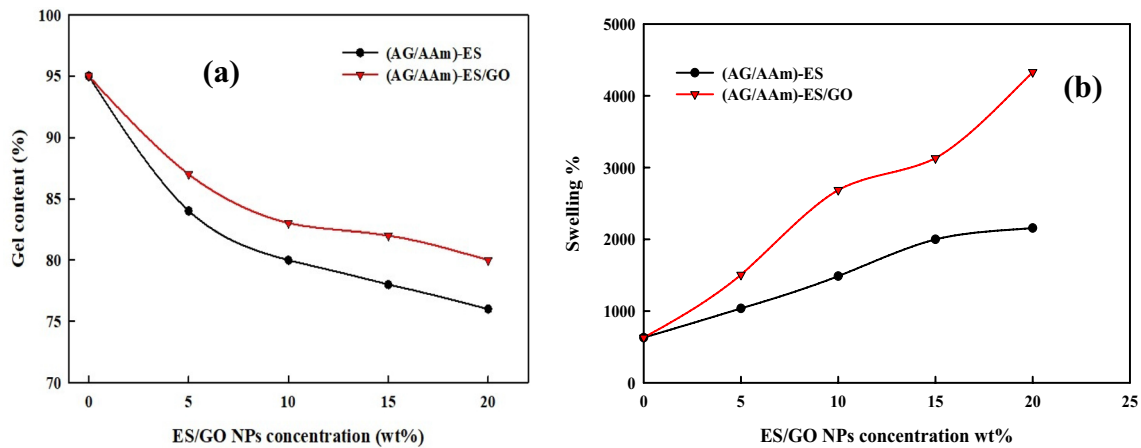

Fig. 8 Effect of **a** total concentration in the feed solution on the swell- ing percent of (GA/AAm) hydrogel at composition (3:7) wt% at dif- ferent irradiation doses;15, 25 and 35 kGy, **b** effect of AAm concen- tration on the swelling percent of (GA/AAm) hydrogel at total feed concentration; 30 wt% and irradiation dose; 35 kGy

and 1017 cm^{-1} [32]. The (GA/AAm)-ES nanocomposite hydrogel showed new peaks due to the CaO of ES. The small peak at 3647.45 cm^{-1} designated to Ca(OH)$_2$ results from the absorption of CaO into the hydroxyl group of water. The CaO was responsible for the peak of 587 cm^{-1}. The peaks at 3017, 2927, 1652, 1427, 1225, and 1022 cm^{-1} are the same characteristic peaks of (GA/AAm) hydrogel. The shift of these peaks is due to the inclusion of CaO in the polymeric matrix. It is worth noting that the bending vibration of –N–H amide at 1427 cm^{-1} and C–O peaks at 1225 and 1022 cm^{-1} overlap with the peaks of Ca(CO$_3$)$_2$ in ES [35, 41]. The same characteristic peaks of (GA/AAm)-ES/GO nanocomposite hydrogel were observed, indicating overlapping of peaks with the characteristic peaks of GO,

indicating good mixing of ES/GO nanoparticles within the hydrogel network [40]. The peak at 3647 cm^{-1} disappeared GO's presence may be preventing CaO in ES from absorb- ing the hydroxyl ion of water. Finally, The FTIR spectra confirmed the grafting of AAm onto GA and the excel- lent mixing of the nanoparticles with the hydrogel matrix. Figure 11 displays the XRD patterns for (GA/AAm), (GA/ AAm)-ES, and (GA/AAm)-ES/GO nanocomposite hydro- gels. The diffractogram of (GA/AAm) hydrogel appears as an amorphous diffraction peak around two theta equal to 23.5°. The crystalline nature was noticed by the inclusion of ES or ES/GO nanoparticles in (GA/AAm) hydrogel to produce (GA/AAm)-ES and (GA/AAm)-ES/GO nanocom- posites hydrogel, respectively [42]. The diffraction pattern
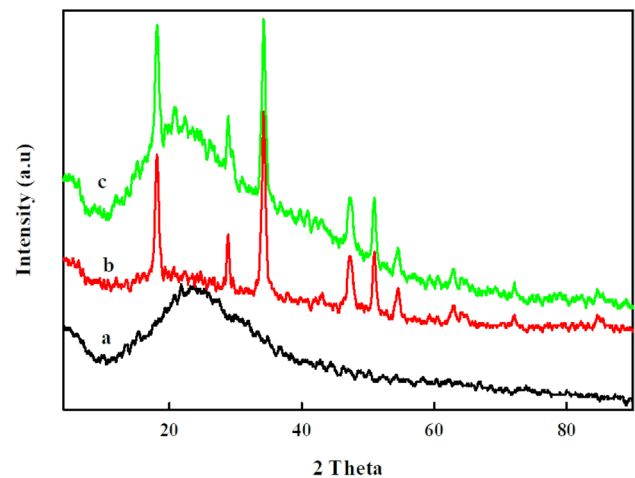
Fig. 9 Effect of ES/GO nanoparticles concentration wt % in the feed solution on the **a** gel content and **b** swelling percentage of (AG/AAm) hydrogel at composition (3:7) wt%, at total concentration (40) wt%, and at different irradiation dose 35 kGy
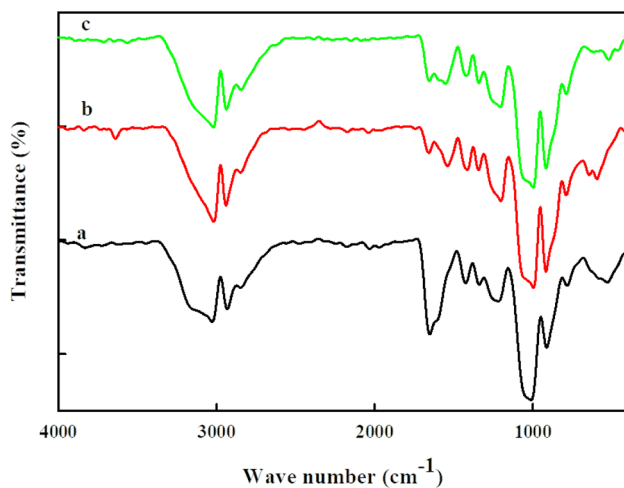
Fig. 10 FTIR spectra of **a** (GA/AAm) hydrogel **b** (GA/AAm)-ES and **c** (GA/ AAm)-ES/GO nanocomposite hydrogels

Fig. 11 XRD patterns of **a** (GA/AAm) hydrogel **b** (GA/AAm)-ES and **c** (GA/ AAm)-ES/GO nanocomposite hydrogels

of (GA/AAm)-ES nanocomposite hydrogel displays all the characteristic peaks of eggshell at two theta 17.7°, 28.83°, 43.45°, 50.545°, 54.545°, 64.43°, 72.54°. After embedding ES/GO into a (GA/AAm) hydrogel structure, the GO characteristic peak at two theta 11.3° vanished, which could be attributed to the complete dispersion of GO in the hydrogel matrix and the formation of a uniform nanocomposite hydrogel. After embedding ES/GO into a (GA/AAm) hydrogel structure, the GO characteristic peak at two theta 11.3° vanished, which could be explained by GO being evenly distributed throughout the hydrogel matrix [43]. While (GA/AAm)-ES/GO nanocomposites exhibits the diffraction peaks of ES. The XRD patterns of (GA/AAm), (GA/AAm)-ES, and (GA/AAm)-ES/GO nanocomposite

hydrogels indicated excellent mixing of ES and ES/GO nanoparticles within the (GA/AAm) hydrogel network.

4.3 Morphology Study

The SEM is a benefit analysis to study the surface morphology of (GA/AAm) hydrogel (GA/AAm)-Es and (GA/ AAm)-ES/GO nanocomposite hydrogels, as seen in Fig. 12. The surface morphology of (GA/AAm) hydrogel, Fig. 12a, appears as an open pore microstructure. The surface possesses high porosity under high magnification due to the hydrophilicity of (GA/AAm) hydrogel. After adding the ES nanoparticles for producing (GA/AAm)-ES nanocomposites hydrogel, Fig. 12b, the morphology of the surface is compactly changed to a rough fracture surface with protrusions. The pore structure disappeared, and ES nanoparticles

Fig. 12 SEM images of **a** (GA/AAm) hydrogel, **b** (GA/AAm)-Es and (**c**) (GA/ AAm)-ES/GO nanocomposite hydrogels
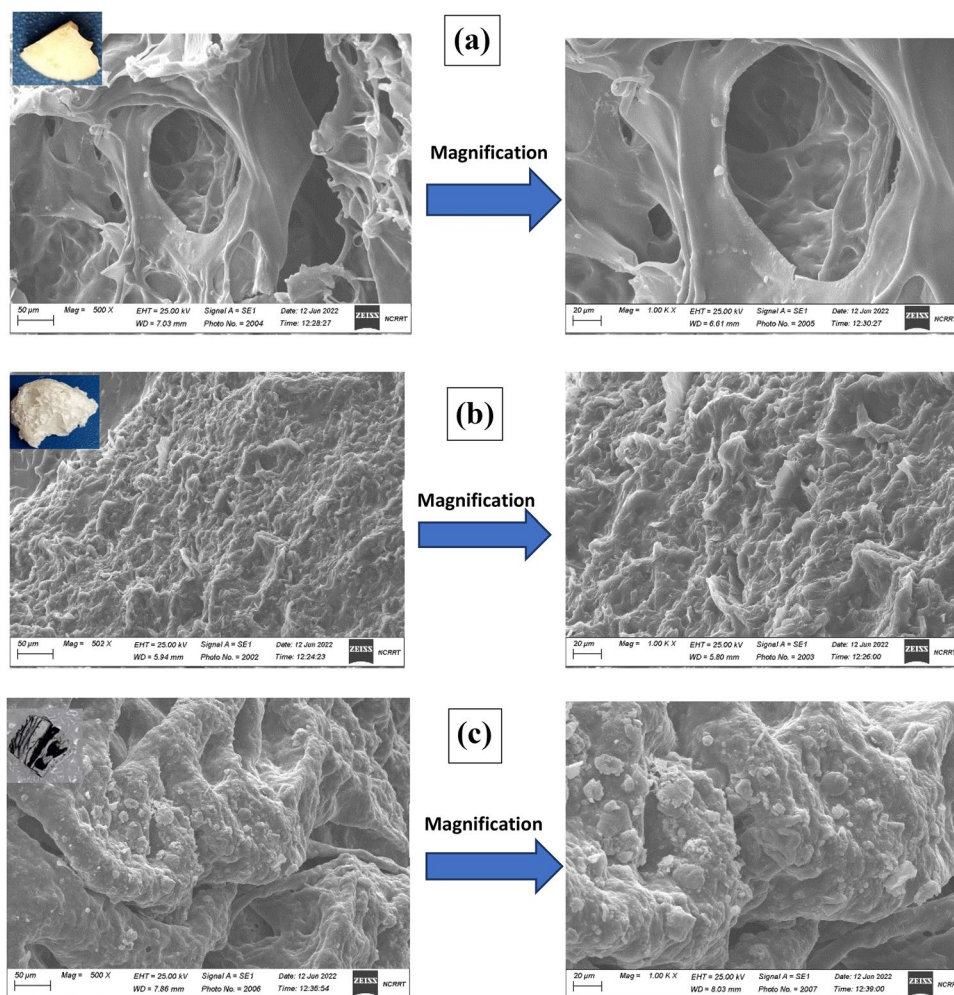
filled the pores and thickness well of the (GA/AAm) hydrogel network. Under a magnification of SEM image of (GA/AAm)-ES nanocomposite, the wall of the network structure becomes dense and thick, indicating the proper mixing of ES with the parent (GA/AAm) hydrogel. SEM image of (GA/AAm)-ES/GO nanocomposite hydrogel observed in Fig. 12c appears a compact surface with a dense network structure of nanocomposite hydrogel resulting in existence of ES and GO nanoparticles dispersed within network hydrogel. Furthermore, the ES nanoparticles precipitated in the hydrogel matrix, and the GO causes the dense network of (GA/AAm) nanocomposites hydrogel in a magnification SEM image.

4.4 Thermal Study

The very important tools for investigating the thermal durability of (GA/AAm) and (GA/AAm)-ES/GO nanocomposites hydrogels using the thermal gravimetric analysis TGA with temperatures up to 600 °C. The TGA thermogram of (GA/AAm) hydrogel seemed four decomposition stages of weight loss, as represented in Fig. 13. The first
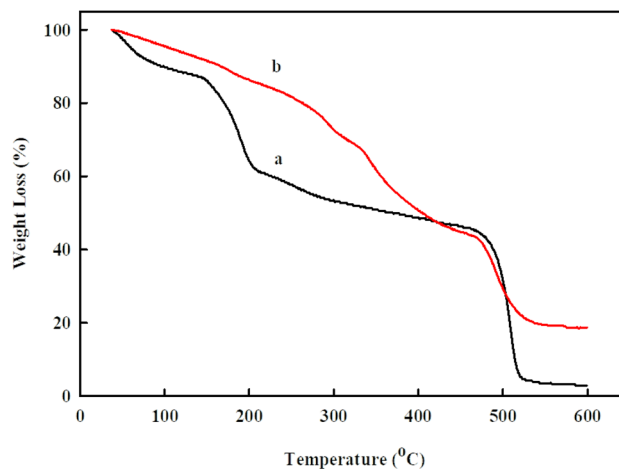

Fig. 13 the thermal stability of **a** (GA/AAm) hydrogel and **b** (GA/AAm)-ES/GO nanocomposites hydrogel

decomposition stage up to 150 °C, is owing to the loss of moisture and volatile compounds. The second thermal decomposition stage, from 150 to 200 ºC, is related to the dehydration of bonded water in (GA/AAm) hydrogel. The third stage from 200 to 450 ºC was attributed to decarboxylation reactions and decomposition of the reactive side groups in (GA/AAm) hydrogel. At 450 ºC the fourth decomposition of the polymer backbone begins, and the weight loss increases rapidly. Finally, the TGA curve reaches a plateau of 520 ºC when all the polymer has decomposed into volatile hydrocarbons and carbon dioxide with a weight loss percentage of 98% [8]. The presence of ES and GO nanoparticles increases the thermal stability of (GA/AAm) hydrogel as represented in the TGA decomposition curve of (GA/AAm)-ES/GO in Fig. 13. It can be noted that the thermal stability (GA/AAm)-ES/GO nanocomposite hydrogel enhanced at the temperature range from 50 to 400 ºC. The thermal stability seems like (GA/AAm) hydrogel in the temperature range of 400–500 ºC. On the other hand, the weight residue is about 19%.

4.5 Adsorption Study

The effect of adsorbent weight on qe and removal percent was seen in Fig. 14. q_e decreases with increasing the weight of the nanocomposite from 5.0 to 10.0 g. q_e was dropped from 10 to 3.8 mg/g (decrease ~ 65%) for (GA/AAm), 17.1 to 5.1 mg/g (decrease ~ 70%) for (GA/AAm)-ES, and 21 to 7 mg/g (decrease ~ 67%) for (GA/AAm)-ES/GO. On the other hand, a little removal effectiveness was observed by increasing the adsorbent weight from 5.0 to 10.0 g. The removal percentage was enhanced from 60 to 70% (increase ~ 17%) for (GA/AAm), 70 to 74% (increase ~ 6%) and (70 to 83) % (increase ~ 19%) for (GA/AAm)-ES/GO.
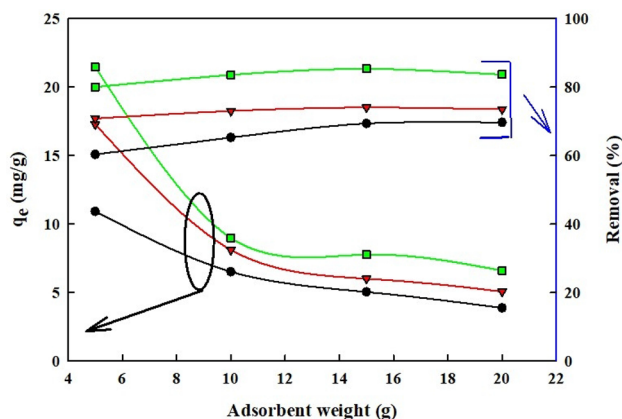
Fig. 14 the effect of Adsorbent weight (g) in one liter onto qe mg/g and removal % of AR dye of (●) (GA/AAm), (▼) (GA/AAm)-ES, and (■) (GA/AAm)-ES/GO nanocomposite hydrogels at pH 7 and initial dye concentration 10 mg/L

At low adsorbent weight, the adsorption approaches fast to equilibrium due to osmotic pressure regardless of the available active sites resulting in an efficient usage of adsorption sites. The adsorption capacity steadily declined throughout the adsorption process due to the unsaturation of the adsorbent's active species. The increased surface area and accessible adsorption active site, as well as a function of osmotic pressure, are responsible for the reduction in qe with increasing adsorbent weight [44]. The surface area of the particles decreases as the adsorbent dose is raised, and the adsorbent active sites become saturated, which lowers the adsorption capacity [45, 46]. However, increasing the weight of (GA/AAm), (GA/AAm)-ES, and (GA/AAm)-ES/GO did not effect on removal efficiency because the adsorbent particles clustered and blocked some adsorption sites [47]. It must be noted that the best adsorbent is (GA/AAm)-ES/GO, and the lowest adsorbent was noticed for (GA/AAm) hydrogel.

The existence of ES in the adsorbent as a relatively low-cost material increases the surface area and porosity. It can adsorb the toxic AR dye through ion exchange, coordination, and hydrogen bond [48]. On the other hand, the superior physical and chemical characteristics of GO, including its wide surface area, high porosity surface reactivity, and oxygenated groups (hydroxyl, epoxy, and carboxyl) on its surface, force its usage as an adsorbent [49]. The mixing of ES with GO in (GA/AAm)-ES/GO composite hydrogel improved its adsorption capability due to the dual effect of ES and GO. The GO enhances the adsorption capacity of ES, resulting in π-π or electrostatic interaction and hydrogen bond with AR dye [50].

4.5.1 Influence of pH

The adsorption capacity and removal percent of (GA/AAm), (GA/AAm)-ES, and (GA/AAm)-ES/GO nanocomposite hydrogels against pH are obtained in Fig. 15. The adsorption capacity and removal percent increase as the medium pH rises to pH 9 and then little decrease was done. The adsorption capacity varied from 6.9 to 13 mg/g, 11 to 18 mg/g, and 19 to 23 mg/g for (GA/AAm), (GA/AAm)-ES, and (GA/AAm)-ES/GO hydrogel nanocomposites, respectively, as observed in Fig. 15a. While the removal percent differ from 50 to 70% for (GA/AAm), from 53 to 75% for (GA/AAm)-ES, and from 84 to 97% for (GA/AAm)-ES/GO as seen in Fig. 15b.

Protonation of hydrogen ions of amide groups in acrylamide causes repulsion between anionic adsorption sites of (GA/AAm) and cationic AR dye molecules in strongly acidic solutions, resulting in adsorption capacity and removal percent for (GA/AAm) hydrogel. The amount of total available adsorption sites for AR was decreased by these H + ions, which decreased adsorption capacity and removal. Quite the contrary, the accessibility of active adsorption sites for AR
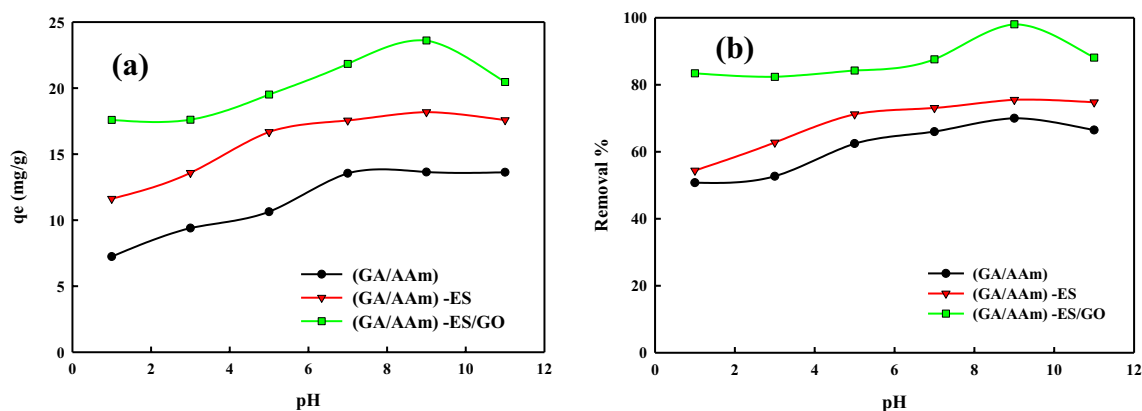
Fig. 15 the effect of pH on **a** q_e mg/g and **b** removal % of (GA/AAm), (GA/AAm)-ES, and (GA/AAm)-ES/GO nanocomposites hydrogel of AR dye at initial concentration 10 mg/L, adsorbent weight 0.1 g in 20 ml dye solution
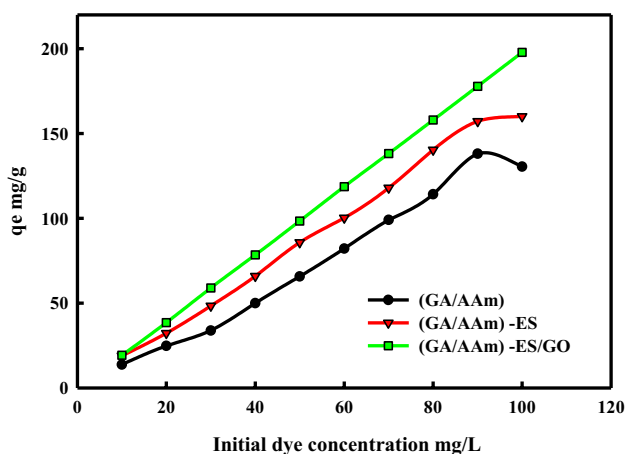
Fig. 16 The q_e as a function of the initial AR dye concentration onto (GA/AAm), (GA/AAm)-ES, and (GA/AAm)-ES/GO nanocomposite hydrogels at adsorbent weight 0.1 g in 20 ml dye solution, pH 9 and at ambient temperature

4.5.2 Effect of Initial Dye Concentration

Figure 16 illustrates the adsorption potential as a function of the initial AR dye concentration by (GA/AAm), (GA/AAm)-ES, and (GA/AAm)-ES/GO nanocomposite hydrogels. When the original dye concentration was increased, an increase in dye adsorption can be seen. As the dye concentration rises, it is thought that more dye molecules will be adsorbed onto the surface of the nanocomposite [54]. The active sites for the adsorption of AR ions getting occupied caused a little drop in the adsorption capacity of (GA/AAm) and (GA/AAm)-ES at 100 mg/L [44]. While the adsorption efficiency for (GA/AAm)-ES/GO nanocomposite hydrogel was raised with the initial dye concentration, this suggested that the quantity of ES/GO nanoparticles increased the surface area and porosity, facilitating the adsorption capacity.
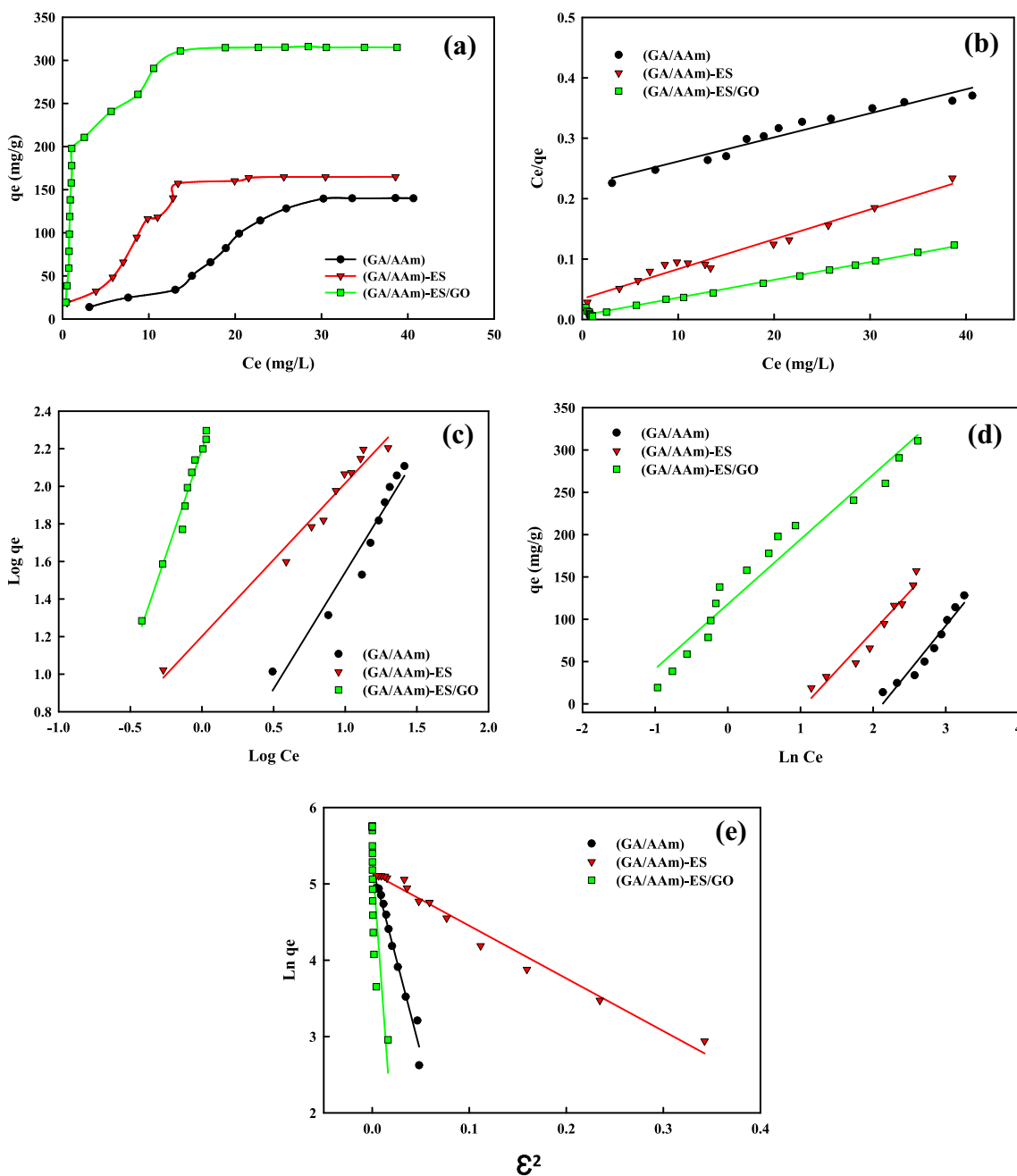
4.5.3 Adsorption Isotherm

The data was examined using the Langmuir, Freundlich, Temkin, and Dubinin-Radushkevich isotherms as shown in Fig. 17. According to the Langmuir adsorption isotherm model, the molecules are transported by equally accessible and energetically equivalent monolayer sites on a homogenous adsorbent surface. The used linear isotherm is expressed by the following Eq. (5):-

$$\frac{C_e}{q_e} = \frac{C_e}{q_{max}} + \frac{1}{k_L q_{max}} \tag{5}$$

where q_e (mg/g) is the equilibrium adsorption quantity of AR dye on the adsorbent, C_e (mg/L) is the equilibrium concentration of AR in the solution, q_{max} (mg/g) is the maximum adsorption amount, and K_L (L/mg) is Langmuir constant related to the energy of the adsorption. Figure 17b shows a

gradually enhanced when the pH of the solution was raised to an alkaline level, resulting in deprotonation and increasing removal percent [44]. For GA/AAm)-ES and (GA/AAm)-ES/GO nanocomposite hydrogels, must be noted the ZPC of (GA/AAm), (GA/AAm)-ES, and (GA/AAm)-ES/GO 7.1 [51], 5.6 and 5.5 [52] respectively, for hydrogel nanocomposites. By increasing the pH, AR dye adsorption onto (GA/AAm)-ES and (GA/AAm)-ES/GO nanocomposite hydrogels is improved. However, at a pH greater than 9, an accumulation of hydroxyl ions in the medium inhibits adsorption on the adsorbent surface. Thus, the AR dye's adsorption efficiency was reduced [53].

Fig. 17 q_e as a function of C_e (**a**), Langmuir (**b**), Freundlich (**c**), Temkin (**d**), and Dubinin–Radushkevich (D-R) (**e**) isotherm models of (GA/AAm), (GA/AAm)-ES, and (GA/AAm)-ES/GO nanocomposites hydrogel for adsorption of AR dye

straight line generated by graphing C_e/q_e versus C_e with R^2 greater than 0.95. The values of q_{max} and K_L were calculated using the slope and intercept of a linear plot, respectively, as stated in Table 1. It was found that the q_{max} value is close to the value of q_{exp}. The separation parameter RL is a dimensionless constant that defines the major characteristics of the Langmuir isotherm (RL). The following Eq. (6) can be used to express this:

$$RL = \frac{1}{(1 + KC0)} \tag{6}$$

where K (l/mg) is the equilibrium constant and C_0 (mg/l) is the initial concentration of the AR dye. The RL value indicates the type and favorability of isotherm to be irreversible (RL = 0), favorable (0 < RL < 1), linear (RL = 1) or unfavorable (RL > 1) [55, 56]. The values of R_L were determined in Table 1.

Table 1 Adsorption isotherm parameters for adsorption of AR by (GA/AAm), (GA/AAm)-ES, and (GA/AAm)-ES/GO nanocomposite hydrogels

Adsorbents	(GA/AAm)	(GA/AAm)-ES	(GA/AAm)-ES/GO
Isotherm models			
Langmuir			
R^2	0.95	0.97	0.99
q_{exp} (mg/g)	139	166	313
q_{max} (mg/g)	169	200	344
K_L (L/mg)	0.01	0.11	0.30
R_L	0.50	0.08	0.03
Freundlich			
R^2	0.95	0.96	0.97
$1/n$	1.24	0.81	2.23
n	0.80	1.23	0.44
Kf (L/mg)	1.99	15.8	15.4
Temkin			
R^2	0.95	0.95	0.95
b (KJ/mol)	23.60	27.10	33.06
Kt (L/mg)	5.79	2.92	4.18
Dubinin–Radush-kevich (D-R)			
R^2	0.97	0.98	0.60
B (mol^{2}J^{-2})	48	6.89	172.4
$qD-R$ (mg/g)	13.0	13.8	14.4

The Freundlich isotherm considers the dye molecules adsorbed on a heterogeneous surface with a non-uniform distribution of adsorption. The linear relationship of Freundlich isotherm adsorption is expressed in Eq. (7): [57]

$$\log q_e = \log K_F + \frac{1}{n} \log Ce \qquad (7)$$

where K_F (L/mg) is the Freundlich constant and $1/n$ is the dimensionless Freundlich intensity parameter that oscillates between 0 and 1. For irreversible processes, $1/n$ equals zero, one for linear processes, between zero and one for favorable processes, and greater than one for unfavorable adsorption processes. The Freundlich constants can be obtained from the slope and intercept of plotting log qe versa log Ce ($R^2 \leq 0.95$) as observed in Fig. 17c.

The Temkin isotherm explains the indirect dye adsorbate interaction with the adsorbent. The linear Temkin equation is expressed in the following Eq. (8):

$$qe = \frac{RT}{bt} lnKt + \frac{RT}{bt} lnCe \qquad (8)$$

where T is the temperature in K, R is the universal gas constant (8.314 J/ mol K), bt is the variation of adsorption

energy (K J/mol) and Kt is the Temkin equilibrium binding constant (L/mg) [58]. b and Kt were ascertained from the slope and the intercept of graphing qe against ln Ce as observed in Fig. 17d with a regression coefficient equal to 0.95 for all systems.

The adsorption of dye molecules within the micropores adsorbent has been described using the Dubinin-Radushkevich (D-R) model. Equation (9) represents this model:

$$\ln qe = \ln q_{DR} - \beta\varepsilon^2 \qquad (9)$$

where q_{DR} is the theoretical adsorption capacity (mg/g), β is the activity coefficient (mol^{2}J^{-2}) related to the adsorption energy, and ε exhibits the Polanyi potential, which is expressed by Eq. (10):

$$\varepsilon = RT \ln \left(1 + \frac{1}{Ce}\right) \qquad (10)$$

The adsorption energy E was estimated from β using the next Eq. (11):

$$E = 1/(2\beta)^{1/2} \qquad (11)$$

The q_{DR} and β were obtained from the slope and intercept of the graphing of lnq_e verse ε^2 with a regression coefficient higher than 0.95 as seen in Fig. 17e.

The Langmuir adsorption isotherm model has the greatest R^2, which is close to one for (GA/AAm)-ES/GO nanocomposite hydrogel ($R^2 = 0.99$). It means AR dye molecules are adsorbed in a monolayer on a homogeneous adsorbent surface. It must be noted that as realized in Table 1 the values of the separation parameter (RL) are 0.50, 0.08, and 0.032 for (GA/AAm), (GA/AAm)-ES, and (GA/AAm)-ES/GO nanocomposites hydrogel, respectively, which mean favorable adsorption for AR dye on all investigated systems. As the value of RL is near zero, more favorable adsorption is done. Thus, the adsorption of AR dye onto (GA/AAm)-ES/GO nanocomposite hydrogel is the best. A comparison between the maximum adsorption capacity of different adsorbents with (GA/AAm)-ES/GO nanocomposite hydrogel adsorbent is shown in Table 2.

4.5.4 Adsorption Kinetics

Figure 18a depicts the adsorption kinetic for (GA/AAm), (GA/AAm)-ES, and (GA/AAm)-ES/GO nanocomposite hydrogels is depicted in. The adsorption capacity increases with the contact time until it reaches a steady state at 480 min. In the initial stage, a high rate of adsorption of AR dye molecules was observed because of the vacant active sites available for binding. With time, the active sites become saturated and exhausted, so a plateau occurred, and the dynamic equilibrium is reached.

Table 2 Comparison between the maximum adsorption capacity of different adsorbents with (GA/AAm)-ES/GO nanocomposite hydrogel adsorbent

Adsorbents	Dye	q max (mg/g)	References
(GA/AAm)-ES/GO	AR	313	Our study
Egg shell powder	Methyl red	1.66	[46]
Egg shell	Congo Red	117.65	[55]
GO/polyaniline	Act acid orange RL (AO-RL)	67.11	[59]
GO/polypyrrole	Act acid orange RL (AO-RL)	71.42	[46]
GO/polystyrene	Act acid orange RL (AO-RL)	58.82	[46]
acrylamide (AM)/starch/graphene oxide (GO) nano sheets and nono-hydroxyapatite (n-HAp)	malachite green	297	[52]
acrylamide/sodium alginate	Crystal violet	1.78	[60]
acrylamide/sodium alginate/2-acrylamido-2-methylpropane sulphonic acid	Crystal violet	3.31	[60]

The kinetic adsorption curves for the adsorption of AR dye onto (GA/AAm), (GA/AAm)-ES, and (GA/AAm)-ES/GO nanocomposite hydrogels were investigated by fitting the experimental kinetics data with different adsorption kinetics models for explaining the adsorption mechanism that rate-determining step.

The Pseudo-first order model is based on the adsorption capacity as seen in Eq. (12) [61]:

$$\text{Log}\left(q_e - q_t\right) = \text{Log } q_e - \frac{k1T}{2.303} \tag{12}$$

where q_t and q_e (mg/g) are the quantity of AR dye adsorbed at time t (min) and equilibrium, respectively, and k_1 (1/min) is the rate constant. The maximum adsorption and rate constant were calculated from the slope and intercept of plotting Log (q_e-q_t) against time with correlation coefficients ($R^2 \geq 0.95$) as seen in Fig. 18b, and Table 2 summarizes the information.the pseudo-second order kinetic models based on the chemisorption mechanism [47]. The linear form of the pseudo-second order kinetics model is:

$$\frac{t}{qe} = \frac{t}{qt} + \frac{1}{k2qe^2} \tag{13}$$

$$h = k_2 q_e^2 \tag{14}$$

where k_2 is the pseudo-second order rate constant (g/mg min) and h is the initial adsorption rate (mg/g min). k_2 and h calculated from the slope and intercept of plotting $\frac{t}{qe}$ and time with regression coefficient ($R^2 \geq 0.95$) as seen in Fig. 18c, and the data are calculated in Table 2.

The Elovich kinetic model is expressed in the following Eq. (15):

$$q_t = \frac{1}{\beta} Ln \ \beta\alpha + \frac{1}{\beta} Ln \ t \tag{15}$$

where α (mg/ g min) is the initial adsorption rate, and β (g /mg) is the desorption constant, which are calculated from graphing of qt against lnt as shown in Fig. 18d, and the data are summarized in Table 2.

Webber-Morris intraparticle diffusion kinetic model is expressed in the following Eq. (16)

$$q_t = K_{id}t^{1/2} + C \tag{16}$$

where K_{id} is the rate constant (mg g^{-1} min$^{1/2}$) and C reflects the boundary layer thickness or surface adsorption. K_{id} and C are calculated from the plotting qt versus $t^{1/2}$ to profit a linear relationship as noticed in Fig. 18e and data are concluded in Table 2. The plot does not pass the origin and has multi-linearity that reflected the complicated stages of the adsorption operation, and confirmed that intraparticle diffusion is not the rate-limiting step [62]. The plot exhibits three stages of adsorptions for (GA/AAm), (GA/AAm)-ES, and (GA/AAm)-ES/GO nanocomposite hydrogels, Fig. 18e. The first linear region was short due to the boundary layer diffusion, which means the AR dye molecules rapidly transfer to the adsorbent surface. The following stage represents intraparticle diffusion where the AR dye enters into the adsorbent pores. The third linear stage is related to the last equilibrium where the intraparticle diffusion dropped. It must be noted that the higher C values indicated a stronger boundary layer impact, indicating that pore diffusion is not the mechanism governing the rate at which the dynamics of the adsorption process occur.

From the summarized data in Table 3, the adsorption process of (GA/AAm), (GA/AAm)-ES, and (GA/AAm)-ES/GO nanocomposite hydrogels are compliable with the pseudo-second-order. Because of the higher regression coefficient and adsorption capacities, q_{cal} is close to q_{exp}. It means that the AR dye molecules are adsorbed on the (GA/AAm), (GA/AAm)-ES, and (GA/AAm)-ES/GO nanocomposite hydrogels surfaces by a chemisorption process.
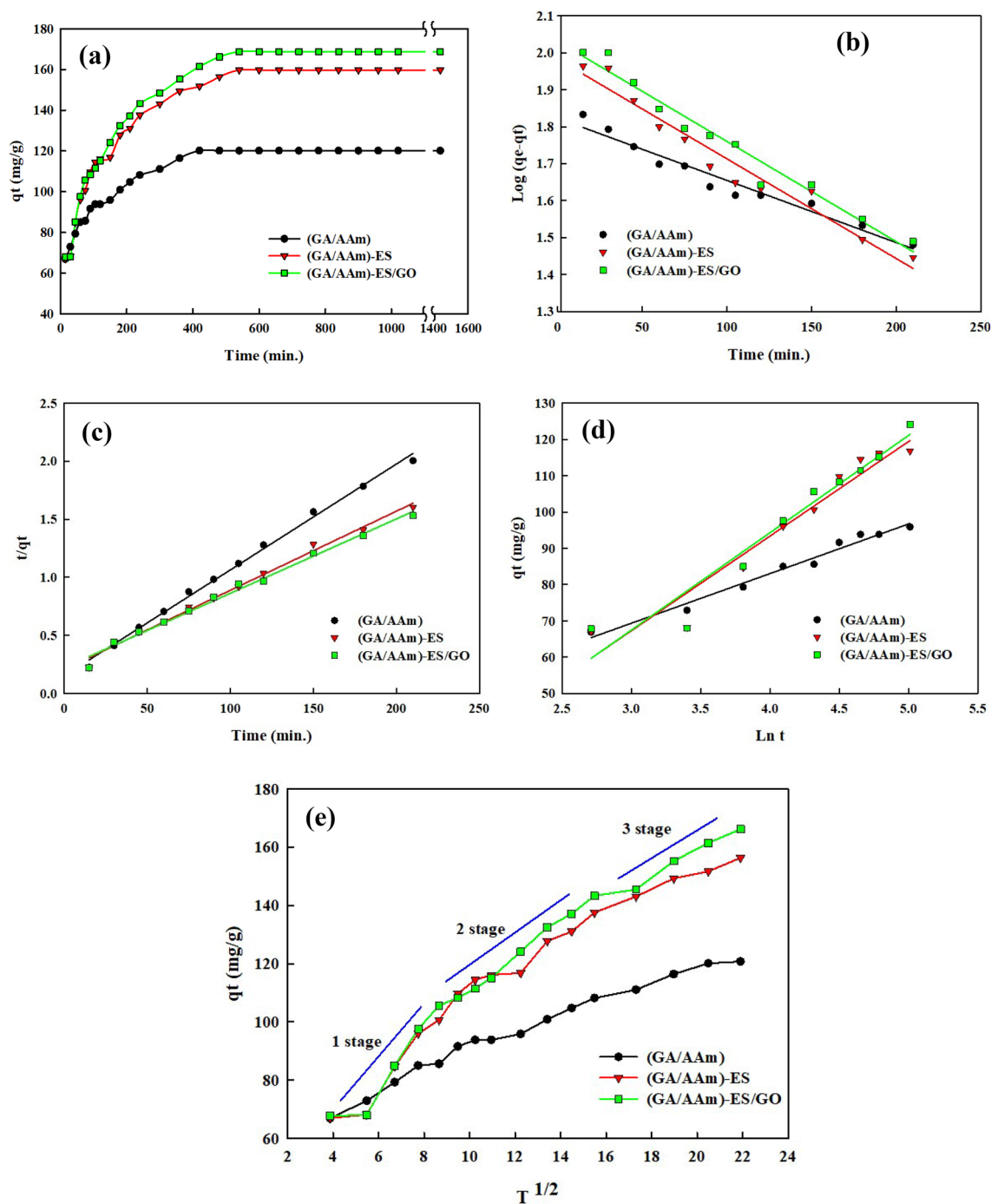
Fig. 18 Effect of time on q_e (**a**), pseudo first order (**b**), pseudo second order (**c**), Elovich (**d**), and intraparticle diffusion (**e**) kinetic models of (GA/AAm), (GA/AAm),-ES, and (GA/AAm)-ES/GO nanocompos-ite hydrogels for adsorption of AR dye at initial dye concentration; 90 mg/L and adsorbent weight 0.1 g in 20 ml dye solution, at pH 9

The calculated initial adsorption rate *h* for (GA/AAm), (GA/AAm)-ES, and (GA/AAm)-ES/GO nanocomposite hydrogels are 3.32, 3.34, and 3.42, respectively. The greatest h that can be given to many unoccupied active sites on the adsorbent surface is (GA/AAm)-ES/GO [54].

4.6 Thermodynamic Studies

The thermodynamic parameters are a valuable factor in the adsorption process. Equation (17) is used to calculate the changes in enthalpy H° (kJ/mol) and entropy S° (kJ/mol.K) [55, 63].

Table 3 Adsorption kinetic data for adsorption of AR dye onto (GA/AAm), (GA/AAm)-ES, and (GA/AAm)-ES/GO nanocomposite hydrogels

Adsorbents	(GA/AAm)	(GA/AAm)-ES	(GA/AAm)-ES/GO
Kinetic models			
Pseudo first order			
R^2	0.98	0.98	0.99
q_{exp} (mg/g)	133	158	168
q_{max} (mg/g)	63	95	107
k_1 (1/min) $\times 10^{-2}$	0.35	0.59	0.62
Pseudo second order			
R^2	0.98	0.99	0.99
q_{exp} (mg/g)	133	158	168
q_{cal} (mg/g)	131	167	178
k_2 (g/mg.min) $\times 10^{-3}$	0. 194	0. 120	0. 108
h (mg/g.min)	3.32	3.34	3.42
Elovich			
R^2	0.95	0.97	0.98
β (g/mg)	0.057	0.053	0.032
A	36.15	53.20	77.70
Intraparticle diffusion			
R^2	0.98	0.95	0.97
C (mg/g)	57.70	54.50	51.21
K_{id} (mg/g.min$^{1/2}$)	3.20	5.053	5.59

$$\ln K_d = \frac{\Delta S}{R} - \frac{\Delta H}{RT} \qquad (17)$$

$K_d = \frac{q_e}{C_f}$ where C_f is the final dye concentration mg/L.

The change in Gibbs free energy $\Delta G°$ (kJ/mol) can be calculated using Eq. (18):

$$\Delta G° = \Delta H° - T\Delta S \qquad (18)$$

The slope and intercept of graphing $\ln K_d$ against $1/T$, as seen in Fig. 19, was used to estimate the change in enthalpy and entropy. The thermodynamic parameters for the adsorption of AR dye molecules onto (GA/AAm), (GA/AAm)-ES, and (GA/AAm)-ES/GO nanocomposite hydrogels surfaces were concluded in Table 4.

Adsorption is exothermic when the value of $\Delta H°$ is negative, whereas endothermic adsorption is indicated by a positive value. The $\Delta H°$ values of AR adsorption onto (GA/AAm) hydrogel are positive at 10 mg/L AR initial concentration and negative at 30 mg/L and 50 mg/L AR initial concentration. As the initial concentration of AR rises, the adsorption changes from being endothermic at 10 mg/L to being exothermic. The change of $\Delta H°$ values from endothermic to exothermic nature of adsorption at higher initial dye concentration may be is a result of the increased interaction between the adsorbent and dye molecules, the higher

driving force for adsorption, and the competition among dye molecules for adsorption sites. For (GA/AAm)-ES and (GA/AAm)-ES/GO nanocomposite hydrogels, $\Delta H°$ values are negative at all investigated initial concentrations. It denoted the exothermic nature of AR adsorption onto (GA/AAm)-ES and (GA/AAm)-ES/GO. On the other hand, the values of $\Delta S°$ are positive for (GA/AAm) and (GA/AAm)-ES at all investigated initial AR concentrations except for (GA/AAm) hydrogel only at 10 mg/L initial AR concentration. It indicates that the adsorption of AR dye molecules onto (GA/AAm), (GA/AAm)-ES, and (GA/AAm)-ES/GO nanocomposite hydrogel surfaces increased the unpredictability at the adsorbent-adsorbate interface [58]. For (GA/AAm)-ES/GO nanocomposite hydrogel $\Delta S°$ values are negative at all investigated initial dye concentrations. It denoted the decrease in randomness at the (GA/AAm)-ES/GO-AR interface. The negative values of $\Delta G°$ for all investigated systems at all temperatures except for (GA/AAm) hydrogel at 10 mg/L initial AR concentration $\Delta G°$ values are positive. $\Delta G°$ negative values refer to the spontaneity, feasibility, and favorable at all temperatures of the adsorption process of AR dye molecules onto adsorbents nanocomposites hydrogel surface [64]. It must be considered that no remarkable increment in the value of $\Delta G°$ at a definite initial dye concentration was obtained by increasing the temperature.

4.7 The Mechanism of Dye Adsorption

The mechanism of the AR dye adsorbed on (GA/AAm)-ES/GO adsorbent occurs in three possible reactions. The first interaction result from the diffusion of AR dye molecules in (GA/AAm)-ES/GO nanocomposites hydrogel network and electrostatic interaction between the dye and the active groups in the polymeric chains may be done. The second type of interaction may occur when AR dye molecules interact with GO via π-π electron interactions between the aromatic groups of AR and GO. The third possible reaction is the AR dye molecules interact with ES via strong H-bonding between ES and AR dye molecules, as shown in Fig. 20.

4.8 Reusability

The sequence reuse for four rounds of (GA/AAm), (GA/AAm)-ES, and (GA/AAm)-ES/GO nanocomposite hydrogels were performed as shown in Fig. 21. It can be seen that high efficiency was observed for (GA/AAm)-ES/GO nanocomposites hydrogel up to three rounds of reuse, with the third cycle having an efficiency of 84.17%. The fourth cycle showed a drop in efficiency of 58.78%. The efficiency of (GA/AAm)-ES nanocomposites hydrogel appears to be good to the twice cycles, where the efficiency was 87.05%. In the third cycle, efficiency was reduced to 55.44%. It should be noted that the efficiency of adsorption for the (GA/AAm)
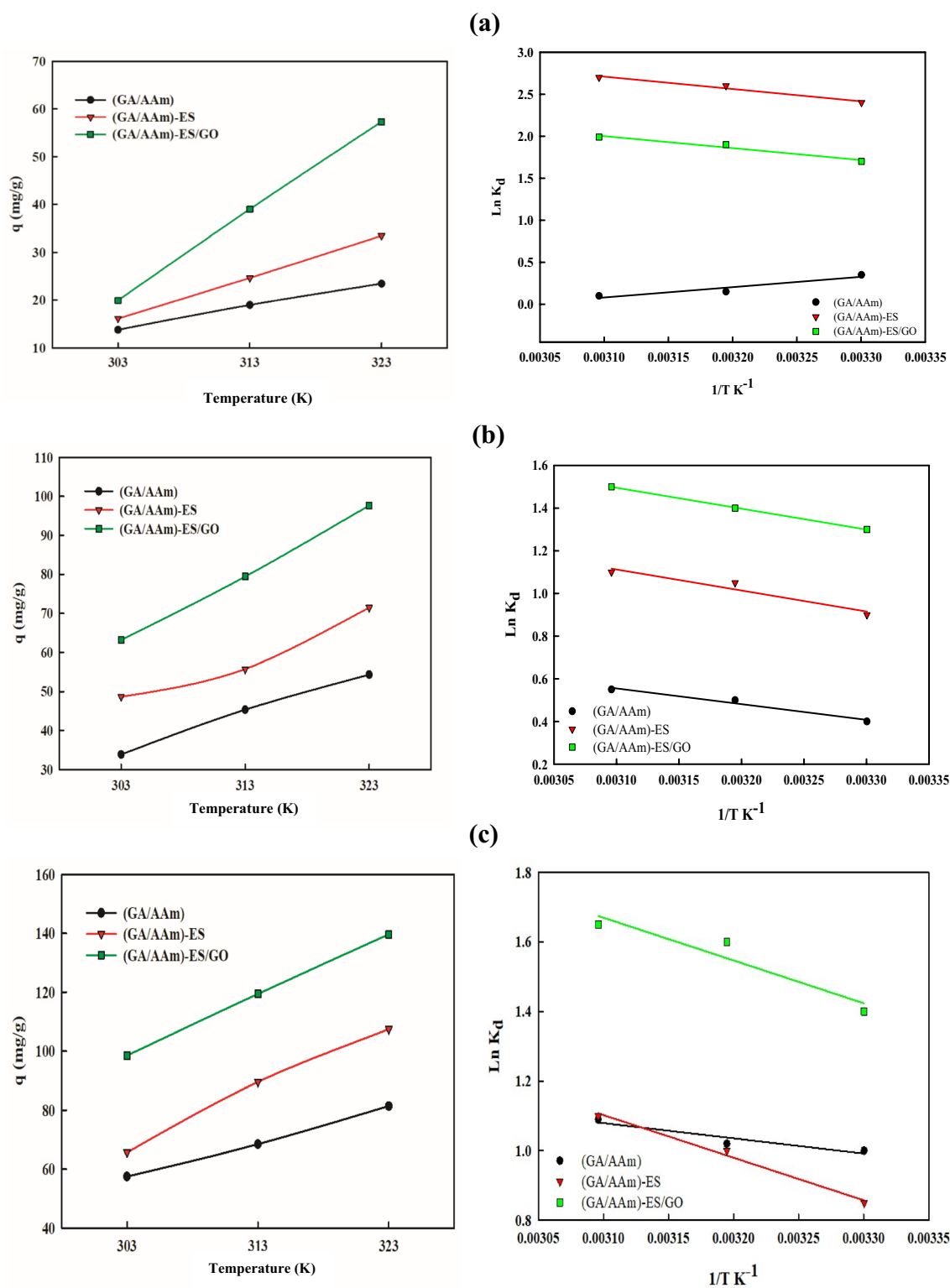
Fig. 19 The adsorption capacity at different temperatures and thermodynamic plots of (GA/AAm), (GA/AAm)-ES and (GA/AAm)-ES/GO nanocomposite hydrogels for adsorption of AR dye at various dye concentrations **a** 10 mg/L, **b** 30 mg/L, **c** 50 mg/L, at adsorbent weight 0.1 g in 20 ml dye solution and pH 9

Table 4 Thermodynamic parameters of (GA/AAm), (GA/AAm)-ES and (GA/AAm)-ES/GO nanocomposites hydrogels for adsorption of AR dye

| Adsorbent	Initial dye conc. mg/L	R^2	$\Delta H°$, kJ/mol	$\Delta S°$, J/molK	$\Delta G°_{303 K}$, kJ/mol	$\Delta G°_{313 K}$, kJ/mol	$\Delta G°_{323 K}$, kJ/mol
(GA/AAm)	10	0.95	14.79	− 0.45	0.284	0.289	0.293
	30	0.97	− 8.85	0.34	− 0.191	− 0.194	− 0.198
	50	0.89	− 5.20	0.29	− 0.139	− 0.142	− 0.145
(GA/AAm)-ES	10	0.97	− 17.70	0.86	− 0.437	− 0.446	− 0.454
	30	0.93	− 11.80	0.50	− 0.269	− 0.274	− 0.279
	50	0.99	− 14.71	0.50	− 0.298	− 0.303	− 0.308
(GA/AAm)-ES/GO	10	0.96	− 17.10	0.77	− 0.404	− 0.412	− 0.419
	30	0.99	− 11.70	0.54	− 0.280	− 0.286	− 0.291
	50	0.90	− 14.70	0.65	− 0.343	− 0.350	− 0.356
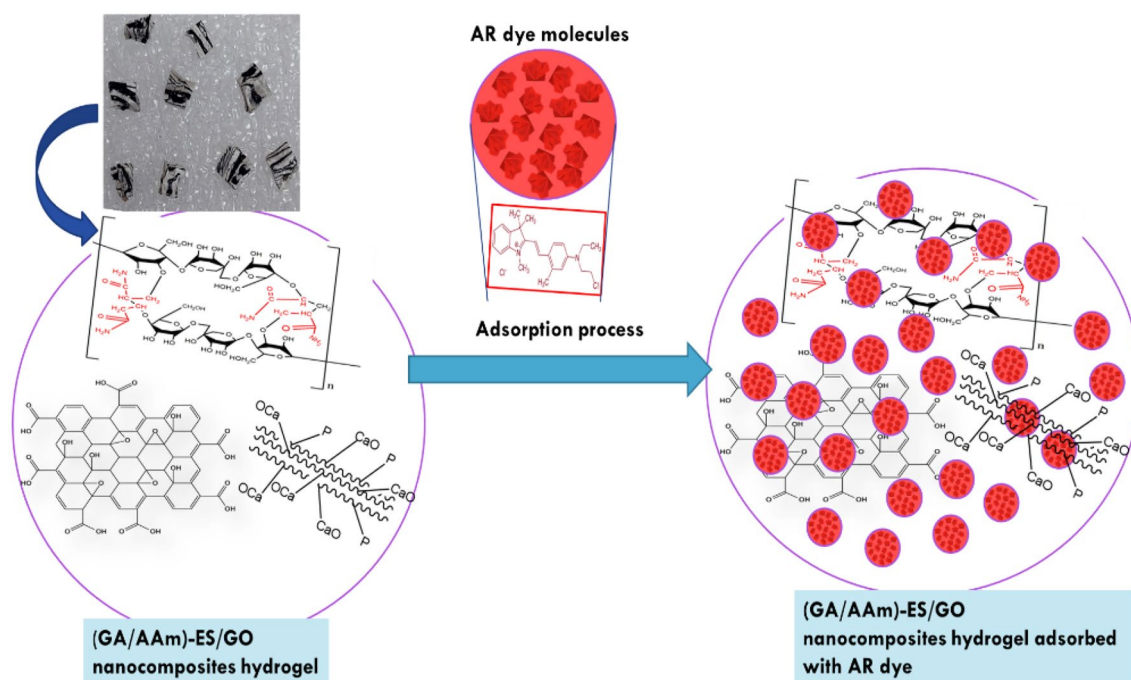
Fig. 20 The possible reaction mechanism for adsorption of AR dye into (GA/AAm)-ES/GO nanocomposite hydrogels

hydrogel decreased to 75% in the first cycle. It may be due to the blocking of active sites on (GA/AAm) hydrogel. (GA/AAm)-ES/GO nanocomposites hydrogel can remove AR dye three times as effectively. It is a viable and cost-effective adsorbent candidate for the treatment of AR dye-contaminated water.

5 Conclusion

Using gamma radiation, a (GA/AAm)-ES/GO nanocomposite hydrogel was successfully created. By raising the total feed concentration and irradiation dose the gel content % was raised while lowering the swelling behavior. The obtained nanocomposite hydrogels were analyzed by FT-IR, XRD, EDX, SEM, and TEM. The outcomes demonstrated that (GA/AAm)-ES/GO had extremely effective Astrazon dye adsorption from contaminated wastewater. It was discovered that the initial pH, starting dye concentration, the dose of (ES/GO), and temperature all had an impact on the adsorption of the AR. Nearly 168 mg/g of AR was adsorbable at the optimum conditions. The experimental results were well suited by the pseudo-second-order adsorption kinetics, and the rate constant was predicted to be $(0.108\ 10^{-3})$ g mg^{-1} min^{-1}. The Langmuir isotherm can provide a good fit for the adsorption equilibrium. At pH 9,
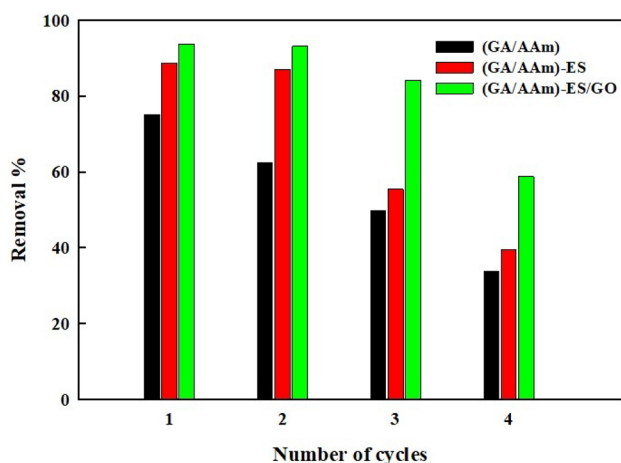
Fig. 21 The reusability of (GA/AAm), (GA/AAm)-ES and (GA/AAm)-ES/GO nanocomposites hydrogels for adsorption of AR dye at initial dye concentration 90 mg/L at Adsorbent weight 0.1 g in 20 ml of dye solution at pH 9

it was reported that the maximal monolayer dye adsorption capacity (qmax) was 313.3 mg/g. The (GA/AAm)-ES/GO nanocomposite can therefore be a suitable choice for the remediation of the fundamentally considered extremely dyes from aqueous solutions. This research will benefit a vast group of scientists working on polysaccharide-based absorption materials and could open up new opportunities for the development of an effective, sustainable, and renewable adsorbent candidate for the removal of organic dyes.

Declarations

Conflict of interest "The authors declare that they have no known competing financial interests or personal relationships that could have appeared to influence the work reported in this paper."

Ethical Approval Not applicable.

Consent to Participate Not applicable.

Consent for Publication Not applicable.

References

1. K.H. Vardhan, P.S. Kumar, R.C. Panda, J. Mol. Liq **290**, 111197 (2019)
2. A. Li, H. Deng, C. Ye, Y. Jiang, ACS Omega **5**, 15152 (2020)
3. S. Mani, R.N. Bharagava, *Recent Advances in Environmental Management*, vol. 47 (CRC Press, 2018)
4. M. Jaishankar, T. Tseten, N. Anbalagan, B.B. Mathew, K.N. Beeregowda, Interdiscip. Toxicol. **7**, 60 (2014)
5. B. Fil, M. Yılmaz, S. Bayar, M. Elkoca, Braz. J. Chem. Eng. **31**, 171 (2014)
6. M.D.N. Ramos, J.P.P. Lima, S.F. de Aquino, A. Aguiar, J Water Process. Engi. **43**, 102273 (2021)
7. A. Sayed, F. Hany, M.E.-S. Abdel-Raouf, G.A. Mahmoud, J. Polym. Res. **29**, 372 (2022)
8. A.S. Al-Gorair, A. Sayed, G.A. Mahmoud, Polymers (Basel) (2022). https://doi.org/10.3390/polym14030567
9. A. Ahmad, D. Jini, A. Mani, C. Parvathiraja, R. Ali, M. Kiyani, A. Alothman, Arab. J. Chem. (2020). https://doi.org/10.1016/j.arabjc.2020.10.002
10. H.R. Osama, A.A. Mohamed, A.M. Ashraf, J. Environ. Sci. **50**, 1 (2021)
11. A. Molla, Y. Li, B. Mandal, S.G. Kang, S.H. Hur, J.S. Chung, Appl. Surf. Sci. **464**, 170 (2019)
12. G.A. Mahmoud, Monatsh. Chem. **145**, 711 (2014)
13. A. Sayed, G.A. Mahmoud, H. Said, A.A. Diab, Mater. Chem. Phys. **280**, 125731 (2022)
14. S. Ahmad, M. Ahmad, K. Manzoor, R. Purwar, S. Ikram, Int. J. Biol. Macromol. **136**, 870 (2019)
15. A. Sayed, M.M. Mohamed, M.E.-S. Abdel-raouf, G.A. Mahmoud, J. Inorg. Organomet. Polym. Mater. **32**, 4589 (2022)
16. M.F. Elshahawy, G.A. Mahmoud, A.I. Raafat, A.E.-H. Ali, E.A. Soliman, J. Inorg. Organomet. Polym. Mater. (2020). https://doi.org/10.1007/s10904-020-01463-3
17. I.H. Alsohaimi, A.M. Nassar, T.A. Seaf Elnasr, B.A. Cheba, J. Clean. Prod. **248**, 119274 (2020)
18. A.K. Sharma, A. Gupta, A. Dhiman, M. Garg, R. Mishra, G. Agrawal, Colloids Surf. A Physicochem. Eng. Asp. **654**, 130155 (2022)
19. Priya, A.K. Sharma, B.S. Kaith, K. Chandel, Vipula, Isha, A. Singh, Mihyi kihfis shishf. Mater. Chem. Phys. **254**, 123304 (2020)
20. M. Rasoulzadeh, H. Namazi, Carbohydr. Polym. **168**, 320 (2017)
21. P. Yılmaz, E. Öztürk, S. Bakirdere, K. Ulgen, B. Özbek, J. Mater. Res. Technol. (2019). https://doi.org/10.1016/j.jmrt.2019.08.043
22. M. Jayanna, H. Bhagyalakshmi, B. Shruthi, M. Veerabhadraswamy, SN Appl. Sci. **3**, 637 (2021)

23. P. Puspitasari, M. Chairil, S. Sukarni, N.S.W. Supriyanto, Mater. Res. Express. **8**, 55008 (2021)

24. N.P. Asri, B. Podjojono, R. Fujiani, R. Nuraini, IOP Conf. Ser. Earth. Environ. Sci. **67**, 12021 (2017)

25. R. Ullah, S.A. Khan, A.A.M. Aladresi, S.A. Alharbi, A. Chinnathambi, Green Chem. Lett. Rev. **13**, 60 (2020)

26. N. Atta, K. Amin, H. El-Rehim, A. Galal, RSC Adv. **5**, 71627 (2015)

27. O. Awogbemi, F. Inambao, E.I. Onuh, Heliyon **6**, e05283 (2020)

28. E.O. Ajala, M.A. Ajala, T.E. Odetoye, F.A. Aderibigbe, H.O. Osanyinpeju, M.A. Ayanshola, Biomass Convers. Biorefin **11**, 2599 (2021)

29. W. Xie, L. Liu, W. Cui, W. An, Materials **12**, 1679 (2019)

30. A.K. Sharma, A. Dhiman, A.K. Nayak, R. Mishra, G. Agrawal, Int. J. Biol. Macromol. **219**, 353 (2022)

31. P. Puspitasari, M. Chairil, S. Sukarni, N. Supriyanto, Mater. Res. Express (2021). https://doi.org/10.1088/2053-1591/ac0266

32. A.I. Raafat, G.A. Mahmoud, T.B. Mostafa, J. Inorg. Organomet. Polym. Mater. **30**, 3116 (2020)

33. Y.H.F. Al-qudah, N.R. Hegazy, G.A. Mahmoud, E.A. Hegazy, Desalination Water Treat **252**, 177–185 (2022)

34. G.A. Mahmoud, A.E.-H. Ali, A.I. Raafat, N.A. Badawy, M.F. Elshahawy, Radiat. Phys. Chem. **147**, 18 (2018)

35. G. Sharma, B. Thakur, A. Kumar, S. Sharma, M. Naushad, F.J. Stadler, Macromol. Mater. Eng. **305**, 2000274 (2020)

36. S. Sharma, K. Virk, K. Sharma, S.K. Bose, V. Kumar, V. Sharma, M.L. Focarete, S. Kalia, J. Mol. Struct. **1215**, 128298 (2020)

37. M.O. Rahman, M.A. Halim, A. Deb, S. Ahmed, M.W. Rahman, N.C. Dafader, S.M.N. Alam, S. Khandaker, M.J. Alam, Adv. Polym. Technol. **2022**, 8405230 (2022)

38. E.E. Khozemy, S.M. Nasef, T.M. Mohamed, J. Inorg. Organomet. Polym. Mater. **30**, 1669 (2020)

39. I. Syed Ahamed Hussain, V. Jaisankar, Polym. Test. **62**, 154 (2017)

40. T. Tolga Demirtaş, A.G. Karakeçili, M. Gümüşderelioğlu, J. Mater. Sci. Mater. Med. **19**, 729 (2008)

41. A.A. Mohamed, G.A. Mahmoud, M.R.E. ElDin, E.A. Saad, Polym.-Plast. Technol. Mater. **59**, 357 (2020)

42. A.M. Elbedwehy, A.M. Atta, Polymers (Basel) **12**, 338 (2020)

43. M. Zhang, Y. Wang, M. Jian, C. Wang, X. Liang, J. Niu, Y. Zhang, Adv. Sci. **7**(6), 1903048 (2020)

44. H. Mittal, A. Al Alili, P.P. Morajkar, S.M. Alhassan, J. Mol. Liq. **323**, 115034 (2021)

45. B. Salunkhe, T. Schuman, Macromol **1**, 256 (2021)

46. S. Rajoriya, V.K. Saharan, A.S. Pundir, M. Nigam, K. Roy, Curr. Res. Green Sustain. Chem. **4**, 100180 (2021)

47. M. Arami, N. Yousefi Limaee, N.M. Mahmoodi, Chemosphere **65**, 1999 (2006)

48. Z.-K. Wang, T.-T. Li, H.-K. Peng, H.-T. Ren, C.-W. Lou, J.-H. Lin, J. Polym. Environ. **30**, 2919 (2022)

49. S. Pashaei-Fakhri, S.J. Peighambardoust, R. Foroutan, N. Arsalani, B. Ramavandi, Chemosphere **270**, 129419 (2021)

50. K. Varaprasad, T. Jayaramudu, E.R. Sadiku, Carbohydr. Polym. **164**, 186 (2017)

51. S. Jabeen, S. Alam, L.A. Shah, M. Zahoor, N.U. Rahman, F.A. Khan, R. Ullah, E.A. Ali, H.C.A. Murthy, A. Sohail, Adsorpt. Sci. Technol. **2022**, 6100791 (2022)

52. H. Hosseinzadeh, S. Ramin, Int. J. Biol. Macromol. **106**, 101 (2017)

53. S. Thakur, S. Singh, B. Pal, Fuel Process. Technol. **213**, 106707 (2021)

54. B. Karagozoglu, M. Tasdemir, E. Demirbas, M. Kobya, J. Hazard. Mater. **147**, 297 (2007)

55. S. Parvin, B.K. Biswas, M.A. Rahman, M.H. Rahman, M.S. Anik, M.R. Uddin, Chemosphere **236**, 124326 (2019)

56. A.K. Sharma, Priya, B.S. Kaith, S. Panchal, J.K. Bhatia, S. Bajaj, V. Tanwar, N. Sharma, J. Environ. Manage. **231**, 380 (2019)

57. A. Shakeri, N. Hazeri, E. Valizadeh, E. Hashemi, A. Kakhky, Iran. J. Chem. Chem. Eng. **31**, 45 (2012)

58. G.M. Taha, E.S. Mansor, M. Sultan, Int. J. Biol. Macromol. **193**, 1859 (2021)

59. S. Noreen, M. Tahira, M. Ghamkhar, I. Hafiz, H.N. Bhatti, R. Nadeem, M.A. Murtaza, M. Yaseen, A.A. Sheikh, Z. Naseem, F. Younas, J. Market. Res. **14**, 25 (2021)

60. U.T. Rehman, S. Bibi, M. Khan, I. Ali, L. Shah, A. Khan, M. Ateeq, RSC Adv. **9**(68), 40051 (2021)

61. G. Ohemeng-Boahen, D.D. Sewu, H.N. Tran, S.H. Woo, Colloids Surf. A Physicochem. Eng. Asp. **625**, 126911 (2021)

62. G.A. Mahmoud, S.F. Mohamed, H.M. Hassan, Desalination Water Treat **54**, 2765 (2015)

63. A. Kumar Sharma, Priya, B. Singh Kaith, S. Bajaj, J.K. Bhatia, S. Panchal, N. Sharma, V. Tanwar, Colloids Surf. B Biointerfaces. **175**, 314 (2019)

64. K. Sharma, S. Sharma, V. Sharma, P.K. Mishra, A. Ekielski, V. Sharma, V. Kumar, Nanomaterials (2021). https://doi.org/10.3390/nano11061403